

ELECTROCHEMISTRY

Stabilization of garnet/Li interphase by diluting the electronic conductor

Wuliang Feng¹, Jiaming Hu², Guannan Qian³, Zhenming Xu⁴, Guibin Zan³, Yijin Liu³, Fei Wang^{1*}, Chunsheng Wang^{5*}, Yongyao Xia^{1*}

The high interfacial resistance and lithium (Li) dendrite growth are two major challenges for solid-state Li batteries (SSLBs). The lack of understanding on the correlations between electronic conductivity and Li dendrite formation limits the success of SSLBs. Here, by diluting the electronic conductor from the interphase to bulk Li during annealing of the aluminium nitride (AlN) interlayer, we changed the interphase from mixed ionic/electronic conductive to solely ionic conductive, and from lithiophilic to lithiophobic to fundamentally understand the correlation among electronic conductivity, Li dendrite, and interfacial resistance. During the conversion-alloy reaction between AlN and Li, the lithiophilic and electronic conductive Li_xAl diffused into Li, forming a compact lithiophobic and ionic conductive Li_3N , which achieved an ultrahigh critical current density of 2.6/14.0 mA/cm² in the time/capacity-constant mode, respectively. The fundamental understanding on the effect of interphase nature on interfacial resistance and Li dendrite suppression will provide guidelines for designing high-performance SSLBs.

INTRODUCTION

Solid-state lithium (Li) batteries (SSLBs) with a ceramic electrolyte receive intense interests as they could deliver both higher energy density and enhanced safety compared with the conventional Li-ion batteries (1–3). Garnet-type solid-state electrolytes (SSEs) [$\text{Li}_7\text{La}_3\text{Zr}_2\text{O}_{12}$ (LLZO)], with an order of magnitude higher shear modulus than metal Li, were once expected to mechanically suppress Li dendrite growth (4, 5). However, the critical current density (CCD) of LLZO is still far below the value of liquid electrolyte (6). The garnet/Li interface usually suffers from high interfacial resistance due to the lithiophobic behavior of the Li_2CO_3 contaminants (7, 8). Although pristine LLZO has been demonstrated to be lithiophilic, Zr^{4+} and doping element such as Al^{3+} or Nb^{5+} are prone to be reduced by metal Li (9), which increase the electronic conductivity and are vulnerable to Li penetration (10).

Li dendrite propagation in LLZO can be either “from inside out” as the higher local electronic conductivity at the grain boundary (11–13) or “from outside in” due to the poor interfacial contacts and instability of the interphase between the garnet electrolyte and metal Li (14). The interphase can be electronic conductive (15–17), ionic conductive (18–21), and mixed conductive (22–26). In principle, SSEs or interphases that are thermodynamically stable against Li will be lithiophobic to Li, while Li wetting (lithiophilic) could be ascribed to the high Gibbs formation energy (27, 28). Electronic conductive graphite or Li alloyable metals are highly reactive with metal Li to form an electronic conductive interphase (ECI), which brings about small area-specific resistance (ASR). Unfortunately, ECI leads to not only Li nucleation on the electronic conductor but also electron

injection into SSEs, resulting in continuous electrolyte degenerations. On the contrary, the ionic conductive interphase (ICI) provides sufficient electron insulativity to prohibit electron attack but usually suffers from lithiophobic behavior (29, 30), the formation of Li-ion resistive by-products (19, 20, 31), low room temperature ionic conductivity (32), and low mechanical strength (33), resulting in a relatively higher ASR. As a compromise, the mixed conductive interphase (MCI) containing both electronic and ionic conductors is developed, which has moderate interfacial overpotential by scaring the electron insulativity. The small electron transfer barrier also provides channels for leakage current to decompose LLZO and increases the electronic conductivity at the grain boundary. Theoretically, an ideal interphase should be thermodynamically stable against Li and contact intimately with high interface energy. However, LLZO is not stable at a negative potential during Li plating, while a thermodynamical stable interphase will probably increase the overpotential. To reduce the overpotential, the interphase should be lithiophilic with mixed or electronic conductivity (34), but such interphases may promote Li dendrite growth (35). Consequently, outstanding lithiophilicity and high capability for Li dendrite suppression seem to be a paradox, and how the conduction types and lithiophobicity of the interphase affect the Li dendrite growth is still unknown.

To realize high capability for Li dendrite suppression, we have to adjust the interfacial electronic and ionic conductivities. However, the widely investigated interphases with different ionic and electronic conductivities are derived from different materials. The diversified electronic and ionic conductivities will cause the large difference in contact resistances and Li nucleation behaviors, thus making it hard to evaluate which conduction type is more suitable for the garnet/Li interphase. To explore the impact of the conduction types on the interfacial stabilities more rigorously, the conduction types should be dynamically changeable and the interphases should be fixed in certain compositions. Up to date, it is still challenging to regulate the distribution of electronic conductor inside the interphases under intimate contact.

Here, we tuned the ionic and electronic conductivities of the garnet/Li interphase under fixed components by annealing the aluminium nitride (AlN) interlayer at 400°C for different durations. During

¹Department of Chemistry, Department of Materials Science, Shanghai Key Laboratory of Molecular Catalysis and Innovative Materials, Fudan University, Shanghai 200433, China. ²Department of Physics, Fudan University, Shanghai 200433, China. ³Stanford Synchrotron Radiation Lightsource, SLAC National Accelerator Laboratory, Menlo Park, CA 94025, USA. ⁴College of Materials Science and Technology, Nanjing University of Aeronautics and Astronautics, Nanjing 210016, China. ⁵Department of Chemical and Biomolecular Engineering, University of Maryland, College Park, MD 20742, USA.

*Corresponding author. Email: yyxia@fudan.edu.cn (Y.X.); cswang@umd.edu (C.W.); feiw@fudan.edu.cn (F.W.)

annealing, AlN reacted with metallic Li, forming a mixed conductive $\text{Li}_3\text{N-Li}_x\text{Al}$ interphase through the conversion-alloy reaction: $\text{AlN} + \text{Li} \rightarrow \text{Li}_3\text{N} + \text{Li}_x\text{Al}$. The electronic conductor Li_xAl gradually diffused into bulk Li due to its higher lithiophilicity than Li_3N , which in situ converted the interphase from mixed conductive to solely ionic conductive. Moreover, the notable lattice expansion of Li_3N made the new interphase dense and intimate with metal Li. The correlation between Li dendrite propagation and the interfacial electronic conductivity was systematically investigated by x-ray photoelectron spectroscopy (XPS), CCD, and COMSOL Multiphysics simulation, confirming that high electronic conductivity in the interphase promoted Li dendrite growth. As the optimized ICI colligated both lithiophobicity and intimate interfacial contact, an ultrahigh CCD of 2.6 mA/cm^2 (time-constant mode) and 14.0 mA/cm^2 (capacity-constant mode) was realized, suggesting that the outstanding Li dendrite suppression benefited from the dilution of the electronic conductor from the interphase.

RESULTS

Tuning the electronic and ionic conductor in the interphase

As shown in the schematic in Fig. 1A, AlN was magnetron-sputtered on Ta-doped garnet electrolyte $\text{Li}_{6.75}\text{La}_3\text{Zr}_{1.75}\text{Ta}_{0.25}\text{O}_{12}$ (LLZTO), transforming the surface of LLZTO from smooth to porous (fig. S1). After the conversion-alloy reaction with metal Li at 400°C for 15 min, LLZTO and Li were intimately contacted due to the volume expansion of the $\text{Li}_3\text{N-Li}_x\text{Al}$ interphase. The interphase that was indexed in fig. S2 was a mixture of ionic (Li_3N) and electronic (Li_9Al_4) conductor, forming a typical MCI (Fig. 1B). As the annealing treatment was prolonged, the Li_9Al_4 electronic conductor diffused from the interphase to bulk Li successively as the high mutual diffusivity between Al and Li, and the volume expansion of Li_3N , forming a transition state interphase (Fig. 1C). Eventually, Al would be infinitely diluted due to the negligible Al mass ratio compared with the bulk Li anode, in situ transforming the interphase from MCI to ICI (Fig. 1D). Molecular dynamics (MD) simulation was carried out to investigate the diffusive behavior of Al in bulk Li. Both 700- and 1000-K MD simulations in fig. S3 demonstrate that Al is highly diffusible in metal Li, and the elevated temperature can further promote the diffusion.

The process of the conduction type transformation can be divided into two steps: a conversion-alloy reaction to form $\text{Li}_3\text{N-Li}_9\text{Al}_4$ composite and a relatively slower process of Li_9Al_4 diffusion. The high porosity of AlN facilitated the infiltration of molten Li under high temperature and pressure, resulting in complete formation of Li_3N that was accompanied with 238% volume expansion (69.9 \AA for AlN and 166.4 \AA for Li_3N , respectively). After substitution of Li from the lattice, Al alloyed with the excessive Li to form Li_9Al_4 and created an Al concentration gradient from the $\text{Li}_3\text{N-Li}_9\text{Al}_4$ interphase to bulk Li anode. Al diffused into bulk Li spontaneously due to the Al concentration gradient, volume expansion of Li_3N , and high lithiophilicity of Li_9Al_4 . Because of the infinitesimal mass ratio compared with Li, Al was eventually “diluted” from the interphase after a long annealing treatment time. By contrast, Li_3N was immoveable due to its high chemical stability with Li and higher lithiophobicity than Li_9Al_4 (27, 36), thus transforming the interphase from MCI to ICI. With a high ionic conductivity of 10^{-3} S/cm and a low electronic conductivity (37, 38), Li_3N provided both fast ionic conductive and electron blocking environment. Density functional theory calculation also demonstrates that Li_3N has more than a 70%

decrease in shear modulus than pristine AlN. Therefore, a softer interphase was created (table S1).

Al diffusion from the $\text{Li}_3\text{N-Li}_9\text{Al}_4$ interphase to bulk Li during annealing at 400°C was demonstrated by elemental line scanning. As shown in Fig. 1E, the plummet of La was related to the surface of LLZTO. After reacting with Li at 400°C for 15 min, the sharp Al peak manifested the high Al content at the interphase. With the increase of annealing treatment duration, the Al peak gradually weakened, which manifested the diffusion of Al into bulk Li. Subsequently, the Al peak almost disappeared when the annealing treatment was extended to 60 min, and finally the scanning curve became flat (120 min), indicating that Al was infinitely diluted from the interphase to the bulk Li anode. Correspondingly, N distance was almost constant and did not change in time due to Al diffusion (fig. S4), manifesting that Li_3N was chemically stable with Li. X-ray computed microtomography in Fig. 1F and line scan of absorption intensity in Fig. 1G demonstrated the evolution of Al concentration from MCI (15 min of annealing treatment) to ICI (120 min of annealing treatment). The absorption gradient at the right edge is related to the decrease of atomic mass, where the slowly reduced absorption curve is referred to the residual Al in the MCI. By contrast, the sharp decrease in ICI manifested the sudden transition from LLZTO to Li_3N or metal Li, indicating that Al had been diluted out of the interphase. The comparison confirmed the successful tuning of the distribution of electronic conductor and lithiophilicity of the interphase.

The contact potential difference (CPD) was used to further verify the electrical potential distribution of MCI and ICI in the vertical section using Kelvin probe force microscopy (KPFM). Because the electronic conductor has a lower potential than the electronic insulator, the dark region corresponded to Li_9Al_4 , while the bright region was in accordance with Li_3N . It is obvious that MCI in Fig. 1H displays an uneven CPD, and the dark region scatters randomly, which probably provided dispersed Li nucleate sites. By contrast, ICI in Fig. 1I shows not only more uniform CPD but also higher average potential according to the line scanning of the CPD, indicating that the electronic conductor had been almost diluted out of the interphase and that the electron tunneling barrier had been significantly increased.

Interfacial resistance evolution with annealing time

The intimate contact of the interphase to both LLZTO and Li was demonstrated by cross-sectional scanning electron microscopy (SEM) and optical images. As shown in Fig. 2A, large gaps were observed between the pristine LLZTO and Li anode due to the lithiophobic Li_2CO_3 surface as evidenced by a large Li contact angle of 152° . After integrating with AlN and reacting with Li, intimate interfacial contact was obtained and the corresponding Li contact angle was reduced to 23° (Fig. 2B). As the transmission electron microscopy (TEM) image of MCI shows in Fig. 2C, the thickness of the MCI was about 150 nm. The region with the highest contrast indicated the fraction of LLZTO, while the closed white dotted line highlighted the dispersed Li-Al alloy. According to the high-resolution TEM image and the corresponding selected-area electron diffraction (SAED) pattern in Fig. 2D, interplanar distances of 2.30 and 4.01 \AA corresponded to (611) and (301) crystal planes of Li_9Al_4 , respectively. The distinct spots in the SAED pattern also indicate that the Li_9Al_4 particle was single crystalline.

The evolution of garnet/Li interfacial resistance during annealing treatment was also characterized by the electrochemical impedance

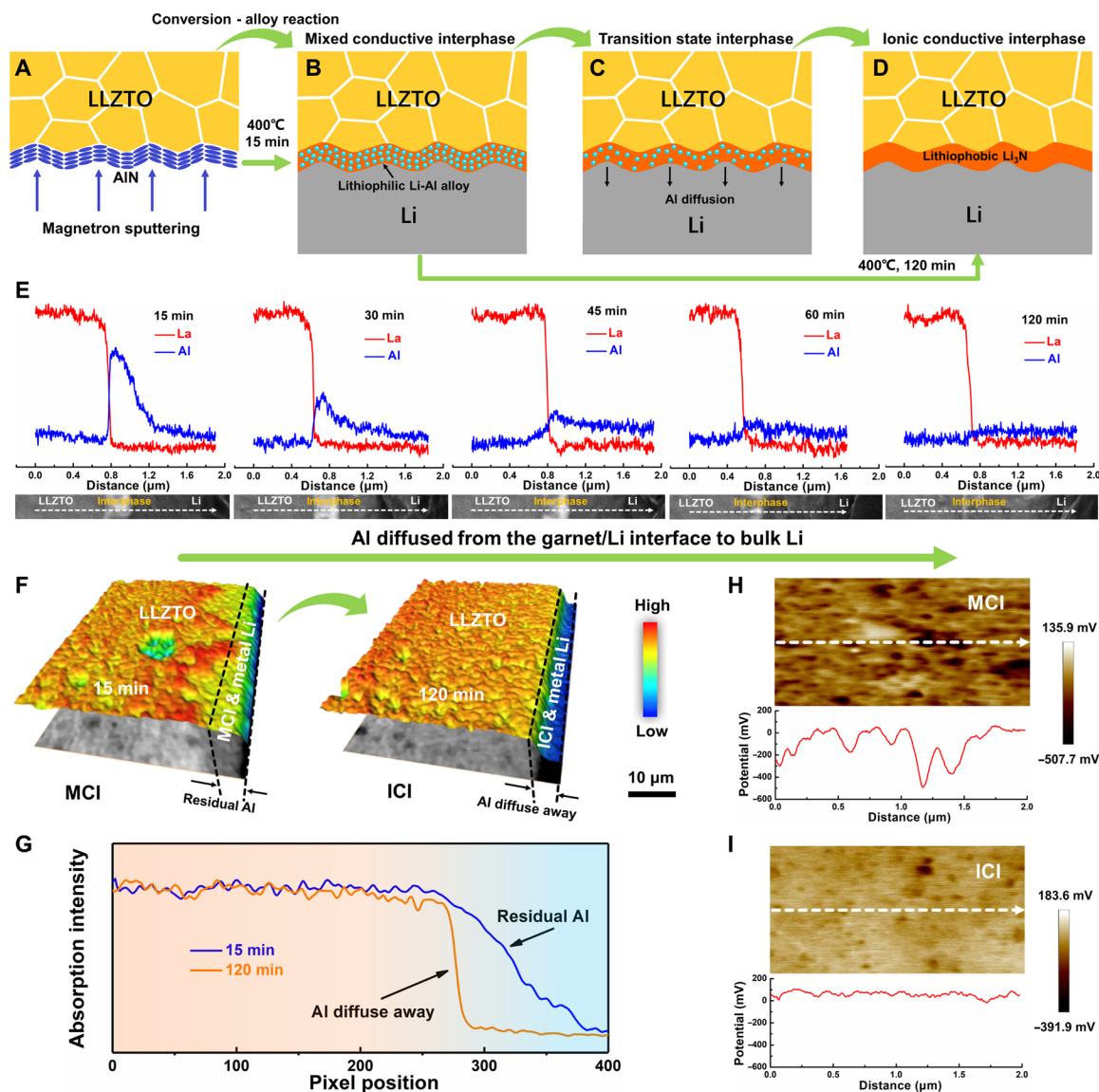


Fig. 1. Characterization of Al diffusion. Schematics of (A) AIN-modified LLZTO, (B) the MCI, (C) the transition state interphase, and (D) the ICI. (E) Elemental line scanning profiles of La and Al at the garnet/Li interphase as reaction time increases. (F) X-ray computed microtomography and (G) absorption intensity of MCI and ICI. CPD analysis of (H) MCI and (I) ICI.

spectroscopy (EIS) profiles of the Li/LLZTO/Li symmetric cells. The pristine-LLZTO/Li interface demonstrated a huge ASR of 1189.3 ohms/cm² (fig. S5). After the 15-min conversion-alloy reaction between AIN and Li, the interfacial resistance was reduced to 173.5 ohms/cm² and contained two resistance arcs (Fig. 2F). Considering that the scattered Li₉Al₄ particles lead to the randomly distributed potentials, the capacitance behaviors of Li₃N/Li₉Al₄ and Li₃N/Li interfaces would also be diversified, which probably led to different response frequencies. As illustrated in the schematic of resistance contributions of MCI (Fig. 2E), R_{int2} represents the interfacial resistance of Li₃N/Li, while R_{in3} is related to Li₃N/Li₉Al₄. Because Li₃N is ultrathin, the bulk and grain boundary resistance can be neglected. The inflexion points of the second arc appeared in the similar frequency regions in the two symmetric cells, which were 775.8 Hz for Li/MCI-LLZTO/Li and 581.6 Hz for Li/ICI-LLZTO/Li (Fig. 2G).

Therefore, it can be deduced that the R_{ct} of Li₃N/Li₉Al₄ emerged in the lower frequency than that of Li₃N/Li. The vanishment of the third arc in the Nyquist plot of Li/ICI-LLZTO-ICI/Li should be explained as the dilution of Li₉Al₄, and the ASR of Li₃N/Li was calculated to be only 30.3 ohms/cm².

The EIS profiles of the symmetric cells with various annealing treatment durations are also compared in fig. S6. It is noticeable that the R_{int3} arc of the symmetric cell after 30 min of annealing treatment shrank significantly, indicating that the concentration of Li₉Al₄ had been greatly reduced. When extended to 60 min, the R_{int3} arc disappeared, demonstrating that Li₉Al₄ almost vanished from the interphase. ASR of bulk garnet, grain boundary, and the overall interphase-LLZTO/Li interface are summarized in fig. S7. It is noticeable that ASR of interphase-LLZTO/Li reduces with the increase of annealing treatment duration due to gradual disappearance of

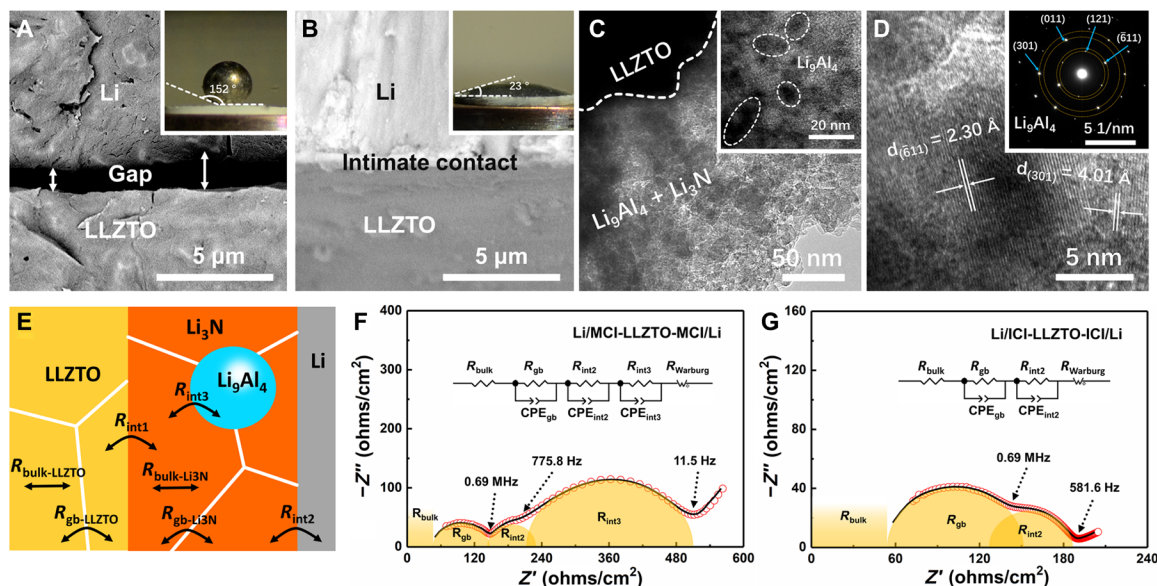


Fig. 2. Distribution of electronic conductor. Cross-sectional SEM images of (A) pristine-LLZTO/Li and (B) interphase-LLZTO/Li interfaces. (C) TEM image of MCI. (D) High-resolution TEM image of Li₉Al₄, with SAED pattern inset. (E) Schematic of resistance contributions in MCI. EIS profiles of (F) Li/ICI-LLZTO-ICI/Li and (G) Li/MCI-LLZTO-MCI/Li symmetric cells.

Li₉Al₄. Nevertheless, the actual ASR of interphase-LLZTO/Li containing Li₉Al₄ should be smaller than the calculated results because the calculation area was based on the cross-sectional area of LLZTO, but the real contact area between Li₃N and Li₉Al₄ can be larger than the cross-sectional area of LLZTO.

Correlation between interphase property and Li dendrite propagation

We investigated how the ionic and electronic conductivities of the interlayer affect the Li plating/stripping. The composition distribution in MCI and ICI after Li plating for 0.1 mAh/cm² was analyzed by XPS at different etching depths. The Li metal was polished clean before the XPS analysis. A total Ar-ion etching time of 45 min was conducted to divide the interphase into 15 signal parts (including some parts of LLZTO). As shown in Fig. 3A, Li 1s XPS spectra of MCI can be divided in three distinguishable zones. In the surface of zone 1, the peak at ~55.2 eV in the first layer can be identified as Li₃N, while it may also contain some Li-Al alloy. As Ar-ion etching went deeper, Li⁰ peak at 52.8 eV (39) slowly emerged in the middle zone 2 and strengthened toward LLZTO, suggesting that Li was mainly plated between LLZTO and the MCI. Last, the main peak shifted to the Li—O bond at 54.5 eV in the deep zone 3, corresponding to the LLZTO. The reason that no Li⁰ signal was detected in zone 1 but noticeable Li⁰ signal was detected in zone 2 should be ascribed to the high electronic conductivity of MCI and its relatively lower ionic conductivity than LLZTO, where MCI functions as the current collector. Consequently, Li plating on the LLZTO surface will reduce the LLZTO at a high Li plating current (overpotential) and promote Li dendrite growth. However, upon further annealing, Li₉Al₄ gradually diffuses into bulk Li, and the function of the Li₃N-Li₉Al₄ interphase layer gradually changed from current collector to electrolyte. Therefore, Li nucleation site will change accordingly from the Li₃N-Li₉Al₄/LLZTO interface and inside the Li₃N-Li₉Al₄ interphase to the surface of bulk Li anode. The changing

of Li nucleation site by transforming the interphase from MCI to ICI was confirmed by the XPS depth profile in Fig. 3B, which consists of only two zones. Zone 1 is Li₃N and zone 3 is LLZTO, indicating that Li only nucleated on the surface of bulk Li anode under the ICI interphase. The comparison of XPS results confirms that the electronic conductor of MCI served as the Li nucleation site to promote Li plating on LLZTO, while the unwanted Li nucleation could be effectively prohibited by an electron insulative, ionic conductive, and lithiophobic Li₃N interphase.

The Li plating sites were also visually observed by a specially designed liquid-based Li symmetric cell. The reason that we used the liquid electrolyte for observing the Li plating site is to provide sufficient convenience to peel off the polypropylene (PP) membrane without damaging the surface of Li disc. As shown in fig. S8, AlN was magnetron-sputtered on Li disc and then annealed at 400°C for 15 and 120 min, respectively. The integration of liquid electrolyte and PP membrane played the same role as the garnet electrolyte. Li discs with the mixed conductive and ionic conductive surface were set as working electrodes with a pure Li disc as counter electrodes. As shown in fig. S9, after Li plating at 1 mAh/cm², the discontinuous metal Li dots can be visually observed on the mixed conductive surface, while the ionic conductive surface still remained clean. This clear and sharp comparison further confirms that Li-ion was reduced inside or on the surface of the MCI but transported smoothly across ICI.

Chronoamperometry analysis was used to quantify the electronic conductivity of the interphases. As illustrated in fig. S10, no evident polarization was observed in the mixed conductive Li₃N-Li₉Al₄ interphase with 15 min of annealing treatment, indicating that electronic flux of MCI dominated the unsteady-state current. The electronic conductivity of MCI was measured to be as high as 3.6×10^{-3} S/cm. As shown in Fig. 3C, when the reaction was extended to 30 min, the polarization occurred and the electronic conductivity markedly decreased to only 7.8×10^{-9} S/cm, manifesting that Li₉Al₄ diffused out of the interphase and a successive electronic blocking region was

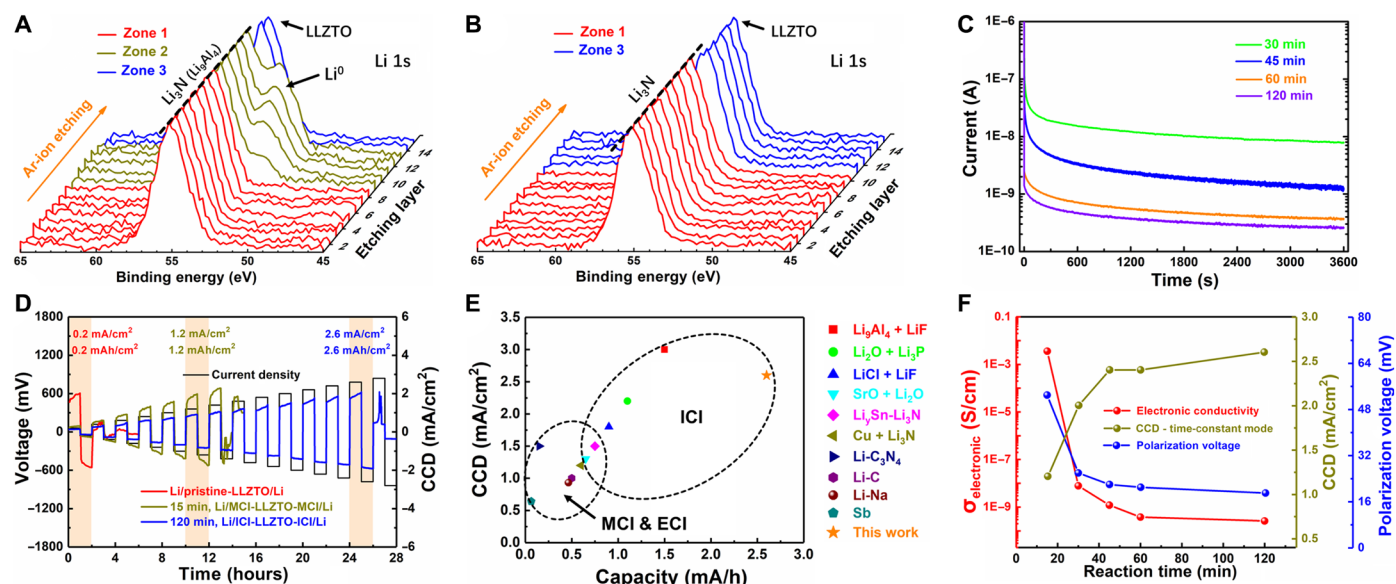


Fig. 3. Impact of electronic conductor on Li dendrite propagation. Li 1s XPS depth profiling analysis of (A) MCI and (B) ICI. (C) DC polarization curve of the interphase with different reaction times. (D) CCD of the Li/pristine-LLZTO/Li, Li/MCI-LLZTO-MCI/Li, and Li/ICI-LLZTO-ICI/Li symmetric cells in the time-constant mode. (E) CCD values in recent literature compared with our work (20, 21, 24, 25, 47–52). (F) AlN/Li reaction time dependence of electronic conductivity, CCD, and polarization voltage.

formed. As the thermal reaction was prolonged to 45, 60, and 120 min, electronic conductivities were 1.2×10^{-9} , 3.8×10^{-10} , and 2.6×10^{-10} S/cm, respectively, which confirmed the conversion from MCI to ICI process due to migration of Al from the interlayer to bulk Li. According to the direct current (DC) polarization curve, the electronic conductivity of the ICI after Al diffusion was six orders of magnitude lower than the MCI. It is also noticeable that the electronic conductivity after 60 min of annealing treatment was quite close to the one after 120 min, indicating that a successive electron blocking Li₃N region had already formed, and the impact of the residual Li₉Al₄ on electrochemical performances of the batteries would be weakened.

CCD of the Li symmetric cells was adopted to evaluate the dendrite suppression capability of the interphases with different conduction types. As shown in Fig. 3D and fig. S11, the CCD at the time-constant mode of Li/Pristine-LLZTO/Li was only 0.2 mA/cm² and then increased to 1.2 mA/cm² for Li/MCI-LLZTO-MCI/Li. As the interphase was transformed from MCI to ICI with 30, 45, and 60, and 120 min of annealing treatment, the CCD values were continuously increased to 2.0, 2.2, 2.2, and 2.6 mA/cm², respectively, indicating that the dilution of the electronic conductor suppressed Li dendrite. The significant increase in CCD by converting the interphase from MCI to ICI demonstrated that preventing the Li plating on the LLZTO surface is critical for stabilizing LLZTO and preventing Li dendrite growth. Figure 3E summarizes the up-to-date CCD values of the Li/garnet/Li symmetric cells with different interphases. It is noticeable that the ICI leads to higher CCD values than MCI and ECI, which is mainly due to the success of electron blocking. As annotated by the pentastar, our work realized not only high CCD value but also the highest critical capacity density (2.6 mAh/cm²), indicating that the in situ formed ICI by diluting the electronic conductor led to the most stable Li/garnet interface. Accordingly, CCD values in the capacity-constant (0.1 mAh/cm²) mode were also investigated and displayed in fig. S12. Li symmetric cells with different

annealing treatment durations showed the values of 8.0 (15 min), 11.0 (30 min), 13.0 (45 min), 14.0 (60 min), and 14.0 mA/cm² (120 min), which were in accordance with the variation trend of the time-constant mode. It should be noted that the real CCD value of Li/MCI-LLZTO/Li may be smaller than that of the results shown here because the contact area between Li₃N and Li₉Al₄ can be larger than the cross-sectional area of LLZTO. However, it is very hard to precisely characterize or calculate the contact area between Li₃N and Li₉Al₄. Consequently, all CCD values were calculated on the basis of the cross-sectional area of LLZTO. In addition, the contact between the ICI and LLZTO is two-dimensional. Therefore, the real contact area should be very close to the cross-sectional area of LLZTO.

Electronic conductivity, CCD value, and polarization voltage as the function of annealing treatment duration are illustrated in Fig. 3F. The main changes occurred in the first 45 min, indicating that the transition from MCI to ICI took at least 45 min at 400°C. It is also apparent to see that both electronic conductivity and the polarization voltage decreased with the prolonging of Al diffusion. Comparatively, CCD was inversely proportional to electronic conductivity and polarization voltage, indicating that Li dendrite growth was in direct correlation with the electronic conductor concentration in the interphase. All these characterizations strongly convince that lowering the interfacial electronic conductivity and a compact but lithiophobic interphase could suppress the Li dendrite propagation, thus demonstrating the validity of the interfacial medication strategy by taking advantage of Al diffusion.

To further understand the impact of electronic conductor on Li dendrite propagation, COMSOL Multiphysics was used to simulate electric potential in MCI and ICI. Figure 4 (A and B) illustrates the simulation models of the MCI and ICI, respectively, where Li₉Al₄ scattered inside Li₃N in either round or irregular shapes. Because of the high crystallinity and rigidity compared with metal Li, grain boundaries and voids were introduced into both LLZTO and Li₃N to provide rooms for the plated Li. Figure 4C shows the electric potential

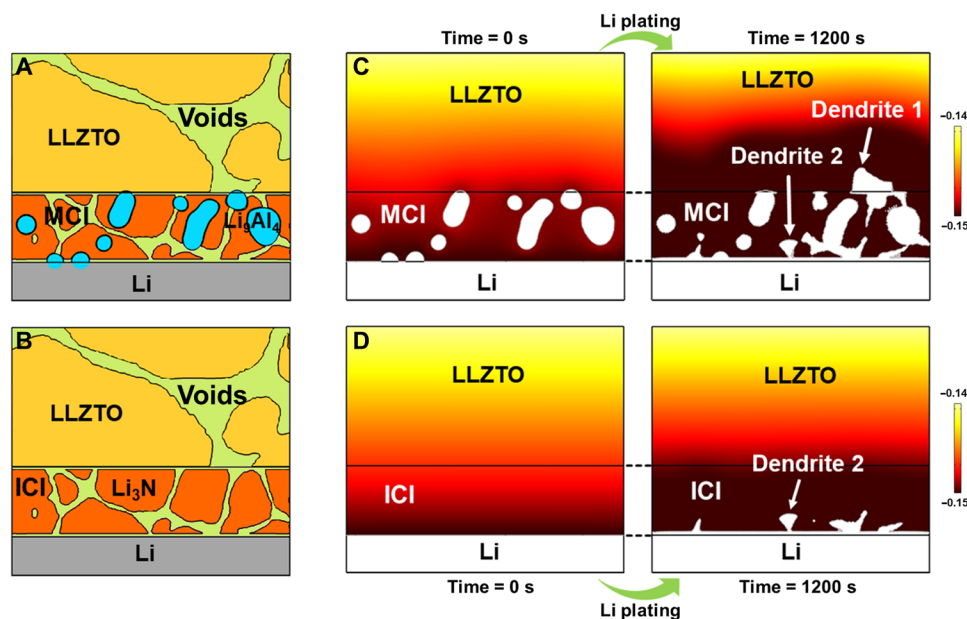


Fig. 4. COMSOL Multiphysics. Schematics of the simulation models: (A) MCI and (B) ICI. Simulation results of electric potential: (C) MCI and (D) ICI.

of MCI before (0 s) and after Li plating (1200 s). The white equipotential region at the bottom and inside of MCI referred to bulk Li and Li_9Al_4 . The randomly distributed Li_9Al_4 led to an uneven electric potential gradient near LLZTO and served as Li nucleation sites to promote Li plating on the surface of LLZTO. The directly contacted Li and LLZTO will induce the reduction of LLZTO and cause Li dendrite growth in the voids of LLZTO (dendrite 1). The growth from the surface of bulk Li anode can also form Li dendrite (dendrite 2). Comparatively, ICI in Fig. 4D displayed a homogeneous electric potential gradient and Li plating only took place on the surface of bulk Li anode.

Because the electronic conductivity of Li_9Al_4 is orders of magnitude higher than Li_3N , the huge difference of dielectric constant would also lead to the distortion of the electric field in MCI. As shown in the simulation result of electric field intensity (fig. S13), Li_9Al_4 led to uniformly distributed electric field intensity in MCI. After Li plating, the sharply decreased electric field intensity in LLZTO indicated that Li nucleated either on the surface of Li_9Al_4 or inside LLZTO. As for ICI, Li_3N and LLZTO have the same electric field intensity. The slightly distorted electric field intensity after Li plating could only be attributed to the plated Li in Li_3N voids, but the electric field intensity inside the LLZTO was kept constant, indicating that Li dendrite propagation was prohibited inside LLZTO. Correspondingly, the temporal evolution of potential difference between the upper and lower boundaries was also illustrated in fig. S14. The distance between the upper boundary and the surface of bulk Li was 300 nm. It is noticeable that high electronic conductivity led to much lower potential difference in MCI (0.769 mV) than in ICI (0.972 mV). As Li plated on the surface of Li_9Al_4 and at the grain boundary of LLZTO, the potential difference in MCI was markedly reduced to 0.024 mV, while the potential difference in ICI was maintained to be as huge as 0.516 mV, further manifesting that the dilution of Li_9Al_4 functioned the interphases from current collector to electrolyte.

The impact of electronic conductor on electrochemical performances

The impact of interphase electronic conductivity on the stability of Li symmetric cell was evaluated. As shown in Fig. 5A, short circuit of Li/Pristine-LLZTO/Li symmetric cell occurred after 93 hours under the current density of 0.1 mA/cm². The Li/MCI-LLZTO-MCI/Li symmetric cell displayed a much smaller initial polarization voltage but increased continuously and suddenly leaped to 400 mV until short circuit took place after 1376 hours. By contrast, the Li/ICI-LLZTO-ICI/Li symmetric cell displayed not only the smallest (~20 mV) but also the most stable overpotential during the 3600-hour cycling. When the current density was 10-fold increased (Fig. 5B), the Li/MCI-LLZTO-MCI/Li symmetric cell showed a higher initial overpotential and short circuited after only 148 hours. In comparison, the overpotential augmentation of Li/ICI-LLZTO-ICI/Li was negligible, indicating that ICI not only was favorable in dendrite suppression but also provided a more stable physical contact.

Garnet/Li contact loss is known to play a key role in the polarization voltage increase. Uneven initial Li plating deteriorates the subsequent Li stripping uniformity, leading to the accumulation of interfacial stress and voids. According to the simulation of the stress distribution in fig. S15, the stress in ICI only increased at the Li_3N /Li interface and the voids of Li_3N after Li plating. By contrast, the existence of Li_9Al_4 led to the markedly increased stress at three parts in MCI: (i) $\text{Li}_3\text{N}/\text{Li}_9\text{Al}_4$ interface, (ii) the voids of LLZTO and Li_3N , and (iii) $\text{Li}_3\text{N}/\text{Li}$ interface. As the temporal changes of the resistance shown in fig. S16, the ASR of the $\text{Li}_3\text{N}/\text{Li}$ interface in both symmetric cells showed a noticeable increase, which was from 37.2 to 63.6 ohms/cm² in Li/MCI-LLZTO-MCI/Li and from 30.3 to 52.9 ohms/cm² in Li/ICI-LLZTO/Li. Comparatively, the ASR of the $\text{Li}_3\text{N}/\text{Li}_9\text{Al}_4$ interface in Li/MCI-LLZTO-MCI/Li showed a much larger increase from 146.9 to 378.5 ohms/cm², which dominated the contact loss in Li/MCI-LLZTO-MCI/Li. During continuous Li plating and stripping, more voids remained on Li_9Al_4 particles than at the $\text{Li}_3\text{N}/\text{Li}$

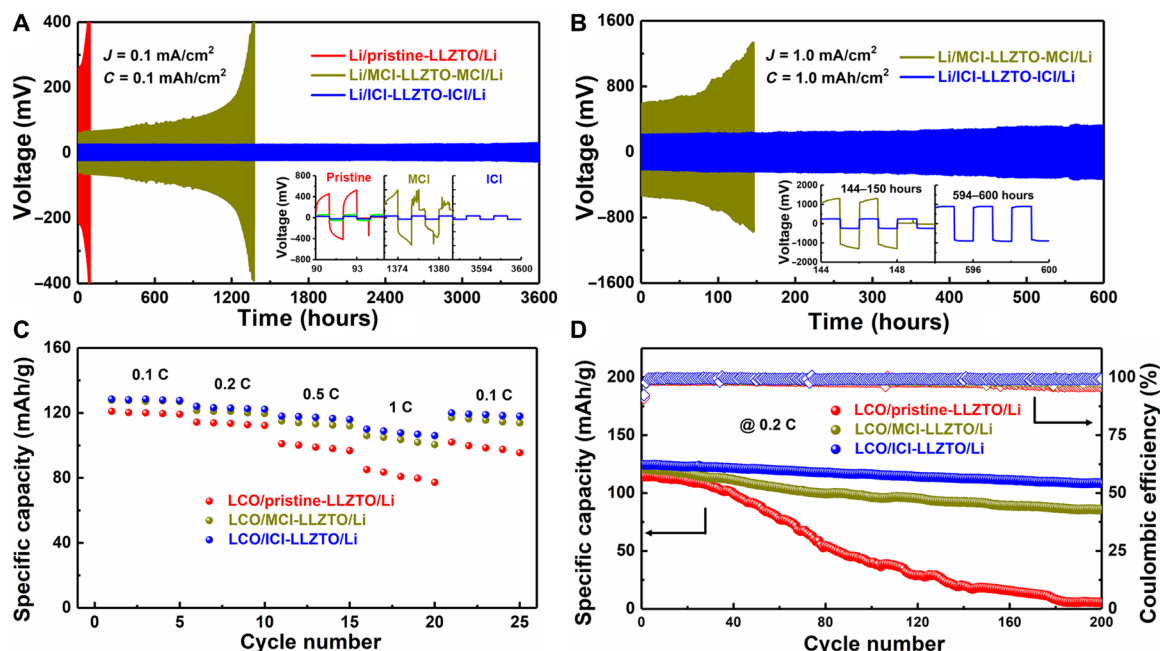


Fig. 5. Battery performances. Galvanostatic cycling of the Li symmetric cells at (A) 0.1 mA/cm² and (B) 1.0 mA/cm². (C) Rate and (D) cycling performances of the LCO/LLZTO/Li hybrid solid-state batteries.

interface, which led to severe contact loss and increased porosity of MCI. Once the voids were irreversible, the local pressure would soar up to potentially crack the interphase or LLZTO, and the local current density would also be increased to facilitate the Li propagation (40, 41).

The hybrid solid-state batteries LiCoO₂ (LCO)/LLZTO/Li with different garnet/Li conduction types had also been assembled to evaluate their application potentials in energy storage devices. To reduce the resistance of the cathode part, toothpaste-like LCO cathode was made by integrating with ionic liquid PY14FSI. As shown in fig. S17, the hybrid solid-state battery with ICI displayed the highest capacity of 124.1 mAh/g at 0.2 C compared with MCI (121.8 mAh/g) and the pristine garnet (114.2 mAh/g). According to the rate performances in Fig. 5C, LCO/pristine-LLZTO/Li displayed the fastest degradation. LCO/MCI-LLZTO/Li showed similar discharge capacities at low rates of 0.1 and 0.2 C with LCO/ICI-LLZTO/Li but decreased faster at a high rate of 0.5 or 1 C, manifesting that the electronic conductor in the interphase was detrimental for the interfacial stability especially at higher current densities. Furthermore, the cyclability of LCO/ICI-LLZTO/Li at 0.2 C also presented the highest capacity retention of 86.6% after 200 cycles (Fig. 5D). In sharp contrast, the capacity retentions of LCO/MCI-LLZTO/Li and LCO/pristine-LLZTO/Li cells were only 70.1 and 5.1%, further corroborating the superiority of the ICI.

DISCUSSION

Li dendrite growth in inorganic SSEs has been extensively investigated during the past decade, while the mechanisms are still under debate. Most Li dendrites propagate from outside in, which is due to the increased overpotential from contact loss during cycling (42, 43), electrolyte reduction (44), and mechanical failure of SSEs (45). In addition, Li is also potentially deposited from inside out as

revealed by neutron depth profiling (11) and garnet bandgap decreasing (46) due to the high electronic conductivity at the grain boundary. In both mechanisms, Li nucleation on the SSE surface will cause the direct contact of SSEs with Li, leading to the electron injection from bulk Li to the SSEs and reduction of SSEs. Consequently, an interphase with sufficient electrical insulation should be the most basic requirement for Li dendrite suppression inside the SSEs.

As the schematic of MCI shown in Fig. 6A, the ultrasmall distance among Li₉Al₄ particles leads to an electron tunneling network from Li to LLZTO. The electron injection would reduce the Zr⁴⁺ and further increase the electronic conductivity, thus lowering the local potential to below 0 V versus Li⁺/Li. Therefore, in the MCI, the Li nucleation spot is determined by the ionic and electronic conductivity and lithiophobicity. When the interphase has a high electronic and a low ionic conductivity, Li deposits between LLZTO and interphase. With a lowered electronic conductivity and an enhanced ionic conductivity, Li may still nucleate inside the interphase, determined by the lithiophobicity of the interphase. When the interphase changed into a fast ionic conductor with sufficient electronic insulativity, Li will deposit on the surface of bulk Li anode.

On the other hand, as shown in Fig. 6B, the electron blocking nature of ICI leads to a huge potential difference between LLZTO and bulk Li, avoiding the reduction of LLZTO. However, the high interface energy of ex situ formed ICI also increased the polarization, forming voids at the interface and facilitating Li dendrite propagation, which was confirmed by the large impedance of Li/Li₃N-LLZTO-Li₃N/Li symmetric cell (fig. S18A). The chemical vapor deposited Li₃N was formed in both α and β phases (fig. S18B). The Li symmetric cell displayed huge polarization voltage (~400 mV) and short circuited at the 159th hour (fig. S18C). The intrinsic lithiophobicity of Li₃N could suppress the dendrite propagation on the aspect of surface energy, and the concomitant huge ASR could also promote

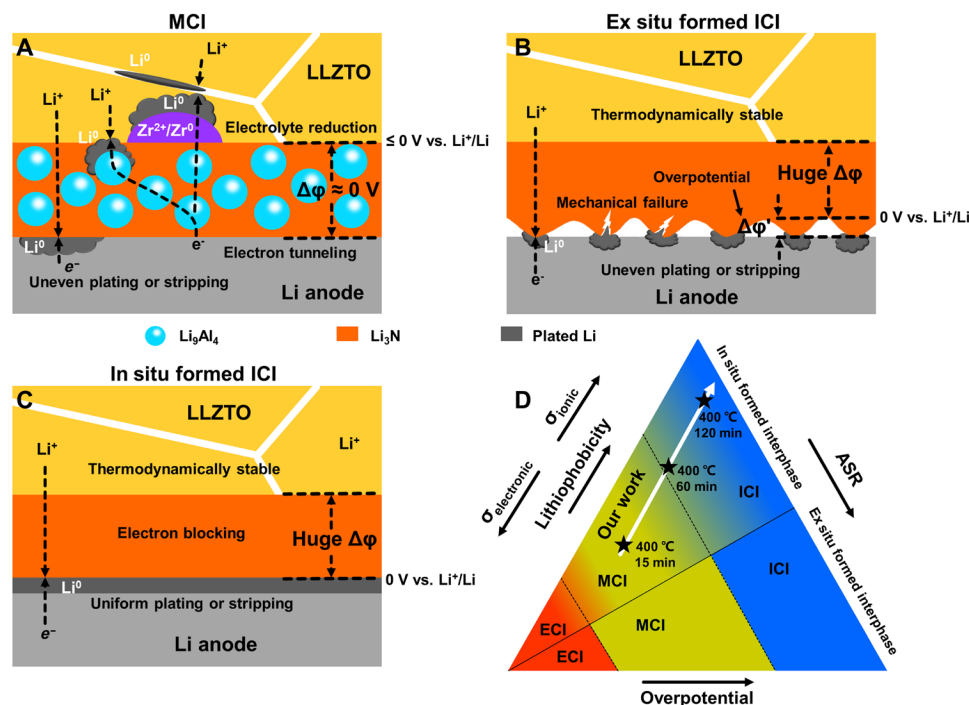


Fig. 6. Detailed schematics of the interphases and design principle. Schematics of the (A) MCI, (B) ex situ formed ICI, and (C) in situ formed ICI. (D) Correlation between the interphase nature (electronic/ionic conductivity, lithiophobicity, overpotential, and ASR) and the Li dendrite growth.

the uneven Li plating, forming the seemingly unsolvable puzzle. The ideal interphase, as shown in Fig. 6C, has long been pursued but was never truly achieved. Through the dynamical evolution from MCI to ICI, the intimate interfacial contact, high ionic conductivity, electronic insulativity, and lithiophobicity were achieved simultaneously in the interphase.

On the basis of the well-controlled comparison, the correlation between the interphase nature and dendrite growth is summarized in the triangle diagram (Fig. 6D). Current methods to suppress Li dendrite are to ex situ form an interphase layer that is either electronic conductive, mixed conductive, or ionic conductive (bottom of the triangle). These “ex situ” interphases with a high electronic conductivity and lithiophilicity (Au, Si, Al, etc.) suffer from the reduction of LLZTO, while the ex situ ICI with a high ionic conductivity, low electronic conductivity, and strong lithiophobicity (Li_3N , LiF , etc.) suffers from poor interfacial contact. The higher ASR and overpotential of the ex situ formed ICI also reduce the cell performance seriously. As a makeshift, MCI was used to compromise Li dendrite growth and cell performance.

To date, it remains very challenging to either in situ or ex situ form an interphase that simultaneously achieves intimate interfacial contact with both SSE and Li, a low electronic conductivity, a high Li-ion conductivity, and strong lithiophobicity. In most cases, the property of the interphase was solely determined by the composition, which corresponds to a single point in the triangle. Different from traditional interphase engineering, our strategy can regulate the ionic/electronic conductivity and lithiophobicity, thus covering a line in the gradient ramp between the in situ formed MCI and ICI in the summarized triangle. As indicated by the white arrow, the initial interphase (400°C , 15 min) was lithiophilic with a highly

electronic conductivity, which induced Li nucleation inside the interphase or LLZTO. With the dilution of the electronic conductor, the ionic conductivity and the lithiophobicity increased, pushing the interphase property to the topline. Meanwhile, the intimate interfacial contact was also maintained due to the volume expansion of Li_3N , making the in situ formed ICI (400°C , 120 min) as the ideal interphase to suppress Li dendrite propagation.

In summary, the controllable evolution of the garnet/Li interphase from mixed conductive to ionic conductive was achieved by diluting the electronic conductor in the interphase through annealing of the AlN interlayer for different durations. The Al concentration gradient, volume expansion of Li_3N , and high lithiophilicity of Li_9Al_4 enabled the in situ formed ICI. Al diffusion was traced by elemental line scanning, x-ray computed microtomography, and MD simulation, manifesting the dilution of the electronic conductor from the interphase. Because the interphase composition was fixed, the interphase nature was simply determined by the distribution of lithiophilic and electronic conductive Li_xAl and lithiophobic and ionic conductive Li_3N . The electronic conductive Li_9Al_4 inside the MCI was demonstrated to be responsible for Li dendrite propagation by reducing the potential in LLZTO and creating non-uniform Li nucleation sites. When Li_9Al_4 was diluted out of the interphase, the as-formed interphase combined both lithiophobicity and stable interfacial contact, thus enabling not only a CCD of $2.6 \text{ mA}/\text{cm}^2$ in the time-constant mode and $14.0 \text{ mA}/\text{cm}^2$ in the capacity-constant mode but also a prolonged electrochemical cycling. The fundamental understanding and the above demonstrations of successful solid-state batteries provide a viable route to optimize the garnet/Li interphase and high-performance solid-state batteries.

MATERIALS AND METHODS

Material synthesis

The LLZTO powder was purchased from Kejing Materials Technology Co. Ltd. The powder was originally pre-prepressed under 30 MPa, followed by hot-press sintering in a graphite die at 1100°C under 60 MPa for 1 hour in argon. The pellet was then sintered at 900°C in air for 1 hour to eliminate the residual graphite on the surface. The as-prepared pellet was finally polished to remove the Li-devoid phase and stored in argon. AlN was magnetron-sputtered on LLZTO pellet with AlN target. Chemical vapor deposition of Li₃N was performed by evaporating pure Li disc in N₂ atmosphere.

Assembly of Li/LLZTO/Li symmetric cell and LCO/LLZTO/Li hybrid solid-state battery

Two Li discs were attached on both sides of the LLZTO pellet. To control the reacting time of AlN and Li precisely, the symmetric cells were not annealed until the panel was heated to 400°C. A pressure of about 5000 Pa was applied to ensure intimate contact between molten Li and LLZTO. With regard to the LCO/LLZTO/Li batteries, the composited cathode consisted of the active material (LCO), conductive agent (Super-P), Li salt (LiTFSI), and ionic liquid (PY14TFSI) in a mass ratio of 12:4:3:29. LiTFSI was first dissolved in PY14TFSI, followed by the integration of Super-P and LCO. The toothpaste-like cathode slurry was blade-coated on LLZTO with a thin poly tetra fluoroethylene die, and the cathode loading was around 5 mg. Stainless steels were attached as current collector. Both symmetric cells and the hybrid solid-state batteries were assembled and tested in Swagelok cells.

Characterizations

The morphology of the cross-sectional images and elemental line scanning of La and Al were characterized by SEM (JOEL JSM6390) and TEM (JOEL JEM2010). The CPD profile of MCI and ICI was characterized by KPFM (Bruker, Dimension ICON). The impedance of the Li symmetric cell and Li₃N film was measured by EIS with a frequency range from 7 MHz to 1 Hz with 50-mV perturbation amplitude (BioLogic, VSP-300). XPS was carried out on an RBD upgraded PHI-5000C ESCA system (PerkinElmer) with Mg K α radiation ($h\nu = 1253.6$ eV). X-ray diffraction pattern was characterized with a Bruker D8 advance diffractometer by Cu K α radiation. X-ray computed microtomography was performed using a Sigray PrismaXRM x-ray microscope (Sigray Inc., Concord, CA, USA). Galvanostatic cycling of Li symmetric cells and Li₂CoO₂/LLZTO/Li battery was operated on LAND CT2001A Battery Cycler (Wuhan, China). Methods of MD simulation and COMSOL Multiphysics are demonstrated in the Supplementary Materials.

SUPPLEMENTARY MATERIALS

Supplementary material for this article is available at <https://science.org/doi/10.1126/sciadv.add8972>

REFERENCES AND NOTES

- M. Armand, J.-M. Tarascon, Building better batteries. *Nature* **451**, 652–657 (2008).
- B. Dunn, H. Kamath, J.-M. Tarascon, Electrical energy storage for the grid: A battery of choices. *Science* **334**, 928–935 (2011).
- J. Janek, W. G. Zeier, A solid future for battery development. *Nat. Energy* **1**, (2016).
- H. Zhang, Y. Chen, C. Li, M. Armand, Electrolyte and anode-electrolyte interphase in solid-state lithium metal polymer batteries: A perspective. *SusMat* **1**, 24–37 (2021).
- Z. Zhang, Y. Shao, B. Lotsch, Y. S. Hu, H. Li, J. Janek, L. F. Nazar, C. W. Nan, J. Maier, M. Armand, L. Chen, New horizons for inorganic solid state ion conductors. *Energy Environ. Sci.* **11**, 1945–1976 (2018).
- A. Jena, Y. Meesala, S.-F. Hu, H. Chang, R.-S. Liu, Ameliorating interfacial ionic transportation in all-solid-state Li-ion batteries with interlayer modifications. *ACS Energy Lett.* **3**, 2775–2795 (2018).
- L. Cheng, E. J. Crumlin, W. Chen, R. Qiao, H. Hou, S. Franz Lux, V. Zorba, R. Russo, R. Kostecki, Z. Liu, K. Persson, W. Yang, J. Cabana, T. Richardson, G. Chen, M. Doeff, The origin of high electrolyte-electrode interfacial resistances in lithium cells containing garnet type solid electrolytes. *Phys. Chem. Chem. Phys.* **16**, 18294–18300 (2014).
- Y. Li, X. Chen, A. Dolocan, Z. Cui, S. Xin, L. Xue, H. Xu, K. Park, J. B. Goodenough, Garnet electrolyte with an ultralow interfacial resistance for Li-metal batteries. *J. Am. Chem. Soc.* **140**, 6448–6455 (2018).
- Y. Zhu, J. G. Connell, S. Tepavcevic, P. Zapol, R. Garcia-Mendez, N. J. Taylor, J. Sakamoto, B. J. Ingram, L. A. Curtiss, J. W. Freeland, D. D. Fong, N. M. Markovic, Dopant-dependent stability of garnet solid electrolyte interfaces with lithium metal. *Adv. Energy Mater.* **9**, 1803440 (2019).
- T. Krauskopf, F. H. Richter, W. G. Zeier, J. Janek, Physicochemical concepts of the lithium metal anode in solid-state batteries. *Chem. Rev.* **120**, 7745–7794 (2020).
- F. Han, A. S. Westover, J. Yue, X. Fan, F. Wang, M. Chi, D. N. Leonard, N. J. Dudney, H. Wang, C. Wang, High electronic conductivity as the origin of lithium dendrite formation within solid electrolytes. *Nat. Energy* **4**, 187–196 (2019).
- Y. Song, L. Yang, W. Zhao, Z. Wang, Y. Zhao, Z. Wang, Q. Zhao, H. Liu, F. Pan, Revealing the short-circuiting mechanism of garnet-based solid-state electrolyte. *Adv. Energy Mater.* **9**, 1900671 (2019).
- F. Aguesse, W. Manalastas, L. Buannic, J. M. Lopez del Amo, G. Singh, A. Llordés, J. Kilner, Investigating the dendritic growth during full cell cycling of garnet electrolyte in direct contact with Li metal. *ACS Appl. Mater. Interfaces* **9**, 3808–3816 (2017).
- C. L. Tsai, V. Roddatis, C. V. Chandran, Q. Ma, S. Uhlenbruck, M. Bram, P. Heitjans, O. Guillon, Li₇La₃Zr₂O₁₂ Interface modification for Li dendrite prevention. *ACS Appl. Mater. Interfaces* **8**, 10617–10626 (2016).
- Y. Shao, H. Wang, Z. Gong, D. Wang, B. Zheng, J. Zhu, Y. Lu, Y. S. Hu, X. Guo, H. Li, X. Huang, Y. Yang, C. W. Nan, L. Chen, Drawing a soft interface: An effective interfacial modification strategy for garnet-type solid-state Li batteries. *ACS Energy Lett.* **3**, 1212–1218 (2018).
- W. Luo, Y. Gong, Y. Zhu, Y. Li, Y. Yao, Y. Zhang, K. (K.) Fu, G. Pastel, C. F. Lin, Y. Mo, E. D. Wachsman, L. Hu, Reducing interfacial resistance between garnet-structured solid-state electrolyte and Li-metal anode by a germanium layer. *Adv. Mater.* **29**, 1606042 (2017).
- K. K. Fu, Y. Gong, Z. Fu, H. Xie, Y. Yao, B. Liu, M. Carter, E. Wachsman, L. Hu, Transient behavior of the metal interface in lithium metal-garnet batteries. *Angew. Chem. Int. Ed. Engl.* **56**, 14942–14947 (2017).
- B. Xu, W. Li, H. Duan, H. Wang, Y. Guo, H. Li, L. Liu, Li₃PO₄-added garnet-type Li_{6.5}La₃Zr_{1.5}Ta_{0.5}O₁₂ for Li-dendrite suppression. *J. Power Sources* **354**, 68–73 (2017).
- Y. Guo, S. Wu, Y.-B. He, F. Kang, L. Chen, H. Li, Q.-H. Yang, Solid-state lithium batteries: Safety and prospects. *eScience* **2**, 138–163 (2022).
- T. Deng, X. Ji, Y. Zhao, L. Cao, S. Li, S. Hwang, C. Luo, P. Wang, H. Jia, X. Fan, X. Lu, D. Su, X. Sun, C. Wang, J.-G. Zhang, Tuning the anode-electrolyte interface chemistry for garnet-based solid-state Li metal batteries. *Adv. Mater.* **32**, 2000030 (2020).
- Y. Ruan, Y. Lu, Y. Li, C. Zheng, J. Su, J. Jin, T. Xiu, Z. Song, M. E. Badding, Z. Wen, A 3D cross-linking lithiophilic and electronically insulating interfacial engineering for garnet-type solid-state lithium batteries. *Adv. Funct. Mater.* **31**, 2007815 (2021).
- J. Gao, J. Zhu, X. Li, J. Li, X. Guo, H. Li, W. Zhou, Rational design of mixed electronic-ionic conducting Ti-doping Li₇La₃Zr₂O₁₂ for lithium dendrites suppression. *Adv. Funct. Mater.* **31**, 2001918 (2021).
- B. Hu, W. Yu, B. Xu, X. Zhang, T. Liu, Y. Shen, Y. H. Lin, C. W. Nan, L. Li, An in situ-formed mosaic Li₃Sn₃/LiF interface layer for high-rate and long-life garnet-based lithium metal batteries. *ACS Appl. Mater. Interfaces* **11**, 34939–34947 (2019).
- H. Huo, Y. Chen, R. Li, N. Zhao, J. Luo, J. G. Pereira da Silva, R. Mücke, P. Kaghazchi, X. Guo, X. Sun, Design of a mixed conductive garnet/Li interface for dendrite-free solid lithium metal batteries. *Energy Environ. Sci.* **13**, 127–134 (2020).
- K. Shi, Z. Wan, L. Yang, Y. Zhang, Y. Huang, S. Su, H. Xia, K. Jiang, L. Shen, Y. Hu, S. Zhang, J. Yu, F. Ren, Y. B. He, F. Kang, In situ construction of an ultra-stable conductive composite interface for high-voltage all-solid-state lithium metal batteries. *Angew. Chem. Int. Ed. Engl.* **59**, 11784–11788 (2020).
- J. Fu, P. Yu, N. Zhang, G. X. Ren, S. Zheng, W. Huang, X. Long, H. Li, X. Liu, In situ formation of a bifunctional interlayer enabled by a conversion reaction to initiatively prevent lithium dendrites in a garnet solid electrolyte. *Energy Environ. Sci.* **12**, 1404–1412 (2019).
- Y. Zhu, X. He, Y. Mo, Origin of outstanding stability in the lithium solid electrolyte materials: Insights from thermodynamic analyses based on first-principles calculations. *ACS Appl. Mater. Interfaces* **7**, 23685–23693 (2015).
- S. H. Wang, J. Yue, W. Dong, T. T. Zuo, J. Y. Li, X. Liu, X. D. Zhang, L. Liu, J. L. Shi, Y. X. Yin, Y. G. Guo, Tuning wettability of molten lithium via a chemical strategy for lithium metal anodes. *Nat. Commun.* **10**, 4930 (2019).

29. Y. Li, B. Xu, H. Xu, H. Duan, X. Lü, S. Xin, W. Zhou, L. Xue, G. Fu, A. Manthiram, J. B. Goodenough, Hybrid polymer/garnet electrolyte with a small interfacial resistance for lithium-ion batteries. *Angew. Chem. Int. Ed. Engl.* **56**, 753–756 (2017).
30. H. Xu, Y. Li, A. Zhou, N. Wu, S. Xin, Z. Li, J. B. Goodenough, Li₃N-modified garnet electrolyte for all-solid-state lithium metal batteries operated at 40 °C. *Nano Lett.* **18**, 7414–7418 (2018).
31. Y. Tian, F. Ding, H. Zhong, C. Liu, Y.-B. He, J. Liu, X. Liu, Q. Xu, Li_{6.75}La₃Zr_{1.75}Ta_{0.25}O₁₂@amorphous Li₃OCl composite electrolyte for solid state lithium-metal batteries. *Energy Stor. Mater.* **14**, 49–57 (2018).
32. H. Duan, Y. X. Yin, Y. Shi, P. F. Wang, X. D. Zhang, C. P. Yang, J. L. Shi, R. Wen, Y. G. Guo, L. J. Wan, Dendrite-free Li-metal battery enabled by a thin asymmetric solid electrolyte with engineered layers. *J. Am. Chem. Soc.* **140**, 82–85 (2018).
33. B. Liu, Y. Gong, K. Fu, X. Han, Y. Yao, G. Pastel, C. Yang, H. Xie, E. D. Wachsman, L. Hu, Garnet solid electrolyte protected Li-metal batteries. *ACS Appl. Mater. Interfaces* **9**, 18809–18815 (2017).
34. R. Chen, Q. Li, X. Yu, L. Chen, H. Li, Approaching practically accessible solid-state batteries: Stability issues related to solid electrolytes and interfaces. *Chem. Rev.* **120**, 6820–6877 (2020).
35. W. L. Huang, N. Zhao, Z. J. Bi, C. Shi, X. X. Guo, L. Z. Fan, C. W. Nan, Can we find solution to eliminate Li penetration through solid garnet electrolytes? *Mater. Today Nano* **10**, 100075 (2020).
36. S. Wenzel, T. Leichtweiss, D. Krüger, J. Sann, J. Janek, Interphase formation on lithium solid electrolytes—An in situ approach to study interfacial reactions by photoelectron spectroscopy. *Solid State Ion.* **278**, 98–105 (2015).
37. K. Iio, A. Hayashi, H. Morimoto, M. Tatsumisago, T. Minami, Mechanochemical synthesis of high lithium ion conducting materials in the system Li₃N-SiS₂. *Chem. Mater.* **14**, 2444–2449 (2002).
38. K. Park, J. B. Goodenough, Dendrite-suppressed lithium plating from a liquid electrolyte via wetting of Li₃N. *Adv. Energy Mater.* **7**, 1700732 (2017).
39. S.-K. Otto, Y. Moryson, T. Krauskopf, K. Peppeler, J. Sann, J. Janek, A. Henss, In-depth characterization of lithium-metal surfaces with XPS and ToF-SIMS: Toward better understanding of the passivation layer. *Chem. Mater.* **33**, 859–867 (2021).
40. Q. Tu, T. Shi, S. Chakravarthy, G. Ceder, Understanding metal propagation in solid electrolytes due to mixed ionic-electronic conduction. *Matter* **4**, 3248–3268 (2021).
41. L. Porz, T. Swamy, B. W. Sheldon, D. Rettenwander, T. Frömling, H. L. Thaman, S. Berends, R. Uecker, W. C. Carter, Y. M. Chiang, Mechanism of lithium metal penetration through inorganic solid electrolytes. *Adv. Energy Mater.* **7**, 1701003 (2017).
42. J. Kasemchainan, S. Zekoll, D. Spencer Jolly, Z. Ning, G. O. Hartley, J. Marrow, P. G. Bruce, Critical stripping current leads to dendrite formation on plating in lithium anode solid electrolyte cells. *Nat. Mater.* **18**, 1105–1111 (2019).
43. M. J. Wang, R. Choudhury, J. Sakamoto, Characterizing the Li-solid-electrolyte interface dynamics as a function of stack pressure and current density. *Joule* **3**, 2165–2178 (2019).
44. T. K. Schwietert, V. A. Arszewska, C. Wang, C. Yu, A. Vasileiadis, N. J. J. de Klerk, J. Hageman, T. Hupfer, I. Kerkamm, Y. Xu, E. van der Maas, E. M. Kelder, S. Ganapathy, M. Wagemaker, Clarifying the relationship between redox activity and electrochemical stability in solid electrolytes. *Nat. Mater.* **19**, 428–435 (2020).
45. Z. Ning, D. S. Jolly, G. Li, R. de Meyere, S. D. Pu, Y. Chen, J. Kasemchainan, J. Ihli, C. Gong, B. Liu, D. L. R. Melvin, A. Bonnin, O. Magdysyuk, P. Adamson, G. O. Hartley, C. W. Monroe, T. J. Marrow, P. G. Bruce, Visualizing plating-induced cracking in lithium-anode solid-electrolyte cells. *Nat. Mater.* **20**, 1121–1129 (2021).
46. X. Liu, R. Garcia-Mendez, A. R. Lupini, Y. Cheng, Z. D. Hood, F. Han, A. Sharafi, J. C. Idrobo, N. J. Dudney, C. Wang, C. Ma, J. Sakamoto, M. Chi, Local electronic structure variation resulting in Li ‘filament’ formation within solid electrolytes. *Nat. Mater.* **20**, 1485–1490 (2021).
47. T. Wang, J. Duan, B. Zhang, W. Luo, X. Ji, H. Xu, Y. Huang, L. Huang, Z. Song, J. Wen, C. Wang, Y. Huang, J. B. Goodenough, A self-regulated gradient interphase for dendrite-free solid-state Li batteries. *Energy Environ. Sci.* **15**, 1325–1333 (2022).
48. X. He, X. Ji, B. Zhang, N. D. Rodrigo, S. Hou, K. Gaskell, T. Deng, H. Wan, S. Liu, J. Xu, B. Nan, B. L. Lucht, C. Wang, Tuning interface lithiophobicity for lithium metal solid-state batteries. *ACS Energy Lett.* **7**, 131–139 (2022).
49. Y. Huang, B. Chen, J. Duan, F. Yang, T. Wang, Z. Wang, W. Yang, C. Hu, W. Luo, Y. Huang, Graphitic carbon nitride (g-C₃N₄): An interface enabler for solid-state lithium metal batteries. *Angew. Chem. Int. Ed. Engl.* **59**, 3699–3704 (2020).
50. J. Duan, W. Wu, A. M. Nolan, T. Wang, J. Wen, C. Hu, Y. Mo, W. Luo, Y. Huang, Lithium-graphite paste: An interface compatible anode for solid-state batteries. *Adv. Mater.* **31**, 1807243 (2019).
51. Y. Zhang, J. Meng, K. Chen, H. Wu, J. Hu, C. Li, Garnet-based solid-state lithium fluoride conversion batteries benefiting from eutectic interlayer of superior wettability. *ACS Energy Lett.* **5**, 1167–1176 (2020).
52. R. Dubey, J. Sastre, C. Cancellieri, F. Okur, A. Forster, L. Pompizii, A. Priebe, Y. E. Romanyuk, L. P. H. Jeurgens, M. V. Kovalenko, K. V. Kravchuk, Building a better Li-garnet solid electrolyte/metallic Li interface with antimony. *Adv. Energy Mater.* **11**, 2102086 (2021).
53. L. Vitos, A. V. Ruban, H. L. Skriver, J. Kollár, The surface energy of metals. *Surf. Sci.* **411**, 186–202 (1998).
54. S. Roy, A. Dutta, N. Chakraborti, A novel method of determining interatomic potential for Al and Al-Li alloys and studying strength of Al-Al₃Li interphase using evolutionary algorithms. *Comput. Mater. Sci.* **190**, 110258 (2021).

Acknowledgments: We would like to thank G. Qian, G. Zan, and Y. Liu at Stanford Synchrotron Radiation Lightsource and Z. Xu at Nanjing University of Aeronautics and Astronautics for their invaluable discussions and help in this work. **Funding:** This work was financially supported by the National Natural Science Foundation of China (nos. 52103335 and 21935003), the China Postdoctoral Science Foundation (no. 2020M681147), Shanghai Science and Technology Committee (19DZ2270100 and 19DZ1205500), Pujiang Talent Program of Shanghai (20PJ1401400), the Open Fund of the Guangdong Provincial Key Laboratory of Advance Energy Storage Materials (grant no. asem202101), and Aerospace Innovation Fund of Shanghai (SAST2020098). **Author contributions:** Y.X., C.W., F.W., and W.F. conceived the work and designed the experiments. W.F. performed the material characterizations and prepared the batteries. J.H. conducted the COMSOL Multiphysics. G.Q., G.Z., and Y.L. organized the x-ray computed microtomography. Z.X. performed the MD simulations. **Competing interests:** The authors declare that they have no competing interests. **Data and materials availability:** All data needed to evaluate the conclusions in the paper are present in the paper and/or the Supplementary Materials.

Submitted 11 July 2022
Accepted 31 August 2022
Published 19 October 2022
10.1126/sciadv.add8972

Stabilization of garnet/Li interphase by diluting the electronic conductor

Wuliang FengJiaming HuGuannan QianZhenming XuGuibin ZanYijin LiuFei WangChunsheng WangYongyao Xia

Sci. Adv., 8 (42), eadd8972. • DOI: 10.1126/sciadv.add8972

View the article online

<https://www.science.org/doi/10.1126/sciadv.add8972>

Permissions

<https://www.science.org/help/reprints-and-permissions>

Use of this article is subject to the [Terms of service](#)

Science Advances (ISSN) is published by the American Association for the Advancement of Science. 1200 New York Avenue NW, Washington, DC 20005. The title *Science Advances* is a registered trademark of AAAS.
Copyright © 2022 The Authors, some rights reserved; exclusive licensee American Association for the Advancement of Science. No claim to original U.S. Government Works. Distributed under a Creative Commons Attribution NonCommercial License 4.0 (CC BY-NC).